# Spin Fine Structure Reveals Biexciton Geometry in an Organic Semiconductor

K. M. Yunusova,[1] S. L. Bayliss,[1,‡] T. Chanelière,[2,3] V. Derkach,[4] J. E. Anthony,[5] A. D. Chepelianskii,[1,*] and L. R. Weiss[6,†,‡]

[1]LPS, University Paris-Sud, CNRS, UMR 8502, F-91405 Orsay, France
[2]Laboratoire Aimé Cotton, CNRS, University Paris-Sud, ENS-Cachan, Université Paris-Saclay, 91405 Orsay, France
[3]University Grenoble Alpes, CNRS, Grenoble INP, Institut Néel, 38000 Grenoble, France
[4]O. Ya. Usikov Institute for Radiophysics and Electronics of NAS of Ukraine 12, Academika Proskury Street, Kharkov 61085, Ukraine
[5]Department of Chemistry, University of Kentucky, Lexington, Kentucky 40506-0055, USA
[6]Cavendish Laboratory, J. J. Thomson Avenue, University of Cambridge, Cambridge CB3 0HE, United Kingdom

(Received 19 March 2020; accepted 25 June 2020; published 27 August 2020)

In organic semiconductors, biexcitons are key intermediates in carrier multiplication and exciton annihilation. Their local geometry governs their electronic properties and yet has been challenging to determine. Here, we access the structure of the recently discovered $S = 2$ quintet biexciton state in an organic semiconductor using broadband optically detected magnetic resonance. We correlate the experimentally extracted spin structure with the molecular crystal geometry to identify the specific molecular pairings on which biexciton states reside.

DOI: 10.1103/PhysRevLett.125.097402

Biexcitons are key excited-state species in a range of nanostructured materials from quantum-confined inorganic systems [1–3] to synthetic molecular structures [4–6]. In organic semiconductors the exciton pair is an intermediate in both the process of singlet fission [7–9]—the formation of a pair of spin-1 (triplet) excitons from an initial spin-0 (singlet) excitation—and its reverse process, triplet-triplet annihilation [10]. While singlet fission is of particular interest for photovoltaics [11–13], where it has been shown to increase efficiencies of solar energy harvesting beyond traditional limits [14,15], triplet-triplet annihilation is of interest for spectral light conversion [10,16], catalysis [17,18], photovoltaics [16,19], and bioimaging [20,21].

Despite their importance, the wave functions of these transient, intermediate pairs remain challenging to probe. Purely optical characterization of biexcitons can be ambiguous as their optical signatures typically overlap with those of singly excited states. Spin resonance has played a key role in showing, unexpectedly, that, in several molecular systems, singlet fission produces both long-lived biexcitons and free triplet excitons and has enabled characterization of the spin properties of both these states [22–26]. An unambiguous signature of biexciton formation is the dominant exchange interaction between the triplets within a pair (parameterized by $J \gtrsim$ THz) [23,27]. This exchange interaction separates the pure singlet ($S = 0$) from the triplet ($S = 1$) and quintet ($S = 2$) pairings of the biexciton by $hJ$ and $3hJ$, respectively, and is identified via spin resonance or magneto-optic spectroscopy [27,28]. We note that the experiments and simulations described here do not depend on the sign of $J$, which we take to be positive [23,27].

Following identification of these biexciton states [23,27], we can now investigate where such bound pairs reside. Conveniently, the ~MHz-GHz spin fine structure of the biexciton is determined by inter- and intratriplet dipolar interactions and therefore provides a native probe of its spatial confinement and orientation [29,30]. We apply this approach in TIPS-tetracene [Fig. 1(b)], a solution-processable singlet fission material of interest for its high singlet fission efficiency [31–33]. TIPS-tetracene is structured with side-chain modification of the canonical fission molecule, tetracene [9]. It crystallizes with four orientationally inequivalent molecules per unit cell [Fig. 1(c)] yielding six possible nearest-neighbor pair sites within a unit cell in addition to noncrystalline defect sites on which biexcitons could reside. Here we measure the spin fine structure in TIPS-tetracene and use it to determine the molecular pair sites where biexcitons reside.

The fine structure is described by the *zero-field splitting* Hamiltonian

$$\hat{H}_{zfs}/h = \mathbf{S}^{\intercal} \cdot \mathbf{D} \cdot \mathbf{S} = D\left(\hat{S}_z^2 - \frac{1}{3}S(S+1)\right) + E(\hat{S}_x^2 - \hat{S}_y^2), \tag{1}$$

where $\mathbf{D}$ is the dipolar tensor ($D$ tensor) with parameters $D$, $E$, and $\mathbf{S}$ is the relevant vector of spin operators (with total spin $S = 1, 2$ for triplet, quintet states) defined along the principal axes ($\hat{x}$, $\hat{y}$, $\hat{z}$) of the $D$ tensor.

We now show how the quintet fine structure ($D_Q$, $E_Q$ and the principal axes $\hat{x}_q, \hat{y}_q, \hat{z}_q$) depends on the underlying triplet pair orientation on two molecules (labeled here

 

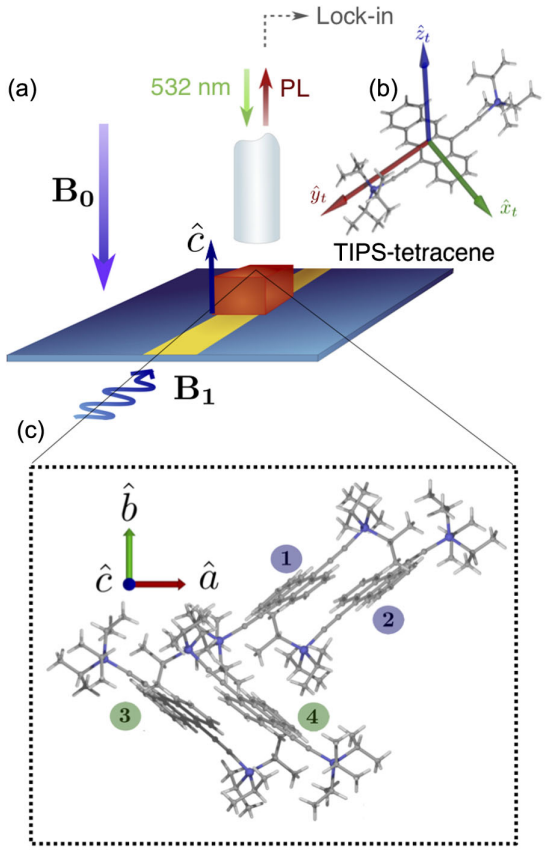


FIG. 1. Broadband ODMR of triplet-pair states. (a) Experimental schematic. Crystalline samples of TIPS-tetracene (oriented with $\hat{c}$ axis as shown) were optically illuminated under amplitude-modulated microwave excitation ($\mathbf{B_1}$) using a broadband strip-line in liquid helium (4 K). PL was collected via optical fiber to detect the microwave-induced change in PL as a function of both microwave frequency and static magnetic field ($\mathbf{B}_0$) with $\mathbf{B}_0 \perp \mathbf{B}_1$. (b) Molecular structure of TIPS-tetracene and corresponding principal axes of the intratriplet dipolar interaction ($\hat{x}_t, \hat{y}_t, \hat{z}_t$). (c) Solid-state crystal structure of TIPS-tetracene with four rotationally inequivalent molecules per unit cell labeled 1–4 and unit cell axes ($\hat{a}, \hat{b}, \hat{c}$).

$a$ and $b$). We assume that each triplet has the same zero-field parameters ($D_T$, $E_T$) and differs only in orientation and position. We define the principal axes of the first triplet state as ($\hat{x}_a, \hat{y}_a, \hat{z}_a$) and the second triplet as ($\hat{x}_b, \hat{y}_b, \hat{z}_b$), defined relative to the molecular structure as in Fig. 1(b) with the vector between them given by $\vec{r}_{ab}$ and unit vector $\hat{u}_{ab} = \vec{r}_{ab}/|\vec{r}_{ab}|$. The zero-field Hamiltonian of the pair in the uncoupled basis is then given by

$$\hat{H}^{(1\otimes1)}_{zfs}/h = \sum_{i=a,b} \mathbf{S}_i^{\intercal} \cdot \mathbf{D}_T^i \cdot \mathbf{S}_i - \Gamma(\hat{u}_{ab} \cdot \mathbf{S}_a)(\hat{u}_{ab} \cdot \mathbf{S}_b) + J\mathbf{S}_a \cdot \mathbf{S}_b \tag{2}$$

where $\Gamma = (3\mu_0\mu_B^2 g^2/4\pi|\vec{r}_{ab}|^3)$ gives the strength of the intertriplet dipolar interaction with $\mu_0$ the magnetic permeability of free space, $\mu_B$ the Bohr magneton, and $g$ the g factor. In the limit of strong exchange coupling ($J \gg D_T$), the Hamiltonian is approximately diagonal in the coupled spin basis defined by the states of pure total spin [27,28,34]. Converting the above Hamiltonian to the coupled basis and projecting into the $S = 2$ subspace gives the quintet zero-field fine-structure Hamiltonian as

$$\hat{H}^{(2)}_{zfs}/h = \mathbf{S}^{\intercal} \cdot \mathbf{D}_Q \cdot \mathbf{S} \tag{3}$$

where $\mathbf{S} = (\hat{S}_x, \hat{S}_y, \hat{S}_z)$ are the Pauli spin operators for total spin-2. The quintet zero-field tensor $\mathbf{D}_Q$ in terms of the underlying triplet fine structure, intertriplet distance, and dipolar interaction is given by

$$\mathbf{D}_Q = \frac{D_T}{6}\left(\sum_{i=a,b} \hat{z}_i\hat{z}_i^{\intercal} - \frac{2}{3}\hat{I}_3\right) + \frac{E_T}{6}\sum_{i=a,b}(\hat{x}_i\hat{x}_i^{\intercal} - \hat{y}_i\hat{y}_i^{\intercal}) - \frac{\Gamma}{3}\left(\hat{u}_{ab}\hat{u}_{ab}^{T} - \frac{1}{3}\hat{I}_3\right), \tag{4}$$

where $\hat{I}_3$ is the identify matrix in three dimensions (a detailed derivation is in the Supplemental Material [35]). Converting $\hat{H}^{(2)}_{zfs}$ to the form of Eq. (1) yields the quintet dipolar parameters $D_Q$, $E_Q$, and the principal axes $\hat{x}_q, \hat{y}_q, \hat{z}_q$ (the eigenvectors of $\mathbf{D}_Q$).

Each distinct potential pair site can be identified by its unique fine-structure parameters in a single crystal with the relation given by Eq. (4). With this motivation we use a macroscopic crystal (∼ mm-scale crystalline domain, see Supplemental Material [35] for details) and measure the principal values and axes of the $D$ tensors of the triplet and quintet states using broadband optically detected magnetic resonance (ODMR).

ODMR measures resonant spin transitions at frequencies determined by the spin parameters of the system (i.e., the spin fine structure). In singlet fission materials, ODMR contrast occurs due to the spin-dependent nature of triplet-triplet recombination to the emissive singlet exciton observed broadly in organic materials [36] (see Supplemental Material [35], Appendix A for details). As described above, the term "fine structure" is used throughout this article to denote the Hamiltonian parameters that set the energy-level splitting within the manifold of triplet-pair and free triplet spin states in the absence of a magnetic field due to dipolar interactions between electrons. In the organic materials relevant for singlet fission, these dipolar interactions are on the MHz–GHz scale and so are probed by their resonant frequency- and field-dependent optical response to microwave radiation.

This experimental setup is shown in Fig. 1(a) and includes 532 nm continuous-wave light excitation, static magnetic field ($\mathbf{B}_0$), and microwave radiation ($\mathbf{B}_1$) with

variable frequency delivered through a broadband copper strip-line. The TIPS-tetracene crystal is aligned with $\mathbf{B}_0 \| \hat{c}$. The ODMR signal is measured by lock-in detection of microwave-induced changes in photoluminescence (PL). While here experiments require magnetic fields of order $D_{T,Q}$, complementary and related techniques measuring static magnetic field effects on PL utilize magnetic fields of order $J$ to measure the magnitude of $J$, extract triplet-pair geometries, and elucidate the role of triplet hopping in pair spin evolution [37,38].

We first perform fixed-frequency (9 GHz), field-swept ODMR. In agreement with previous measurements using transient electron spin resonance, we observe two pairs of spin transitions consistent with the $\Delta m = \pm 1$ transitions of the $S = 1$ triplet exciton (which we label $T^{\pm}$) and the $\Delta m = \pm 1$ transitions of the $S = 2$ quintet state (labeled $Q^{\pm}$), as shown in the Fig. 2(a),(b). (Note that this spectrum confirms the expected orientation of the crystal aligned with $\mathbf{B}_0 \| \hat{c}$ as noted in the Supplemental Material [35]) We correlate these observed high-field transitions with zero-field transitions [magnetic field strength $|\mathbf{B}_0| = 0$, Fig. 2(c),(d)], measured here to sensitively determine the zero-field splitting parameters. We now describe the microwave transitions observed experimentally. Two of the triplet energy levels are separated by $|hD_T|$ from the lowest level, and the two upper eigenstates are further split by $|2E_T h|$ [Fig. 2(c) in blue]. ODMR then occurs at microwave frequencies $\nu = D_T \pm E_T$. The three lowest quintet levels are split by $|D_Q|$ from the ground state to the first two states with a further splitting of $|6E_Q|$ between those two upper levels [Fig. 2(c) in red]. This leads to ODMR transition frequencies at $\nu = D_Q \pm 3E_Q$. Note that the previously reported $D$ parameters for TIPS-tetracene are $D_T \sim 1.4$ GHz and $D_Q \sim D_T/3$ [23,39].

The spectra of triplets and biexcitons can be separated in ODMR using the difference in lifetime of the two species [23,39]. The microwave amplitude modulation frequency (137 Hz) is chosen such that the triplet signal appears with equal amplitude on the in-phase (X-channel) and out-of-phase (Y-channel) lock-in channels, which corresponds to the inverse lifetime of the triplets. The signal from shorter lived biexcitons appears only on the X channel and can be isolated by subtracting X and Y channels. The zero-field X- and Y-channel ODMR spectra are plotted in Fig. 2(d),(e) in black (X channel) and grey (Y channel). The transitions on the Y channel are consistent with triplets with $|D_T| = 1.4$ GHz and $|E_T| = 14$ MHz [Fig. 2(e), with overlaid spectral fit in blue]. Transitions in the frequency region expected for the quintet only appear on the X channel and give $|D_Q| = 477$ MHz and $|E_Q| = 22$ MHz [Fig. 2(d), with overlaid spectral fit in red]. The measurement of the $E$ parameters here is made possible by the reduced linewidths observed at zero field relative to previous measurements under nonzero magnetic field. [Note that the spectral fit in Fig. 2(d) includes a minor species with slightly larger quintet parameters ($|D_Q| = 490$ MHz, $|E_Q| = 24$ MHz) that quickly decays in intensity with field.]

Having extracted the principal values of the triplet and quintet fine structure at zero field, we now map the resonance frequencies as a function of magnetic field to

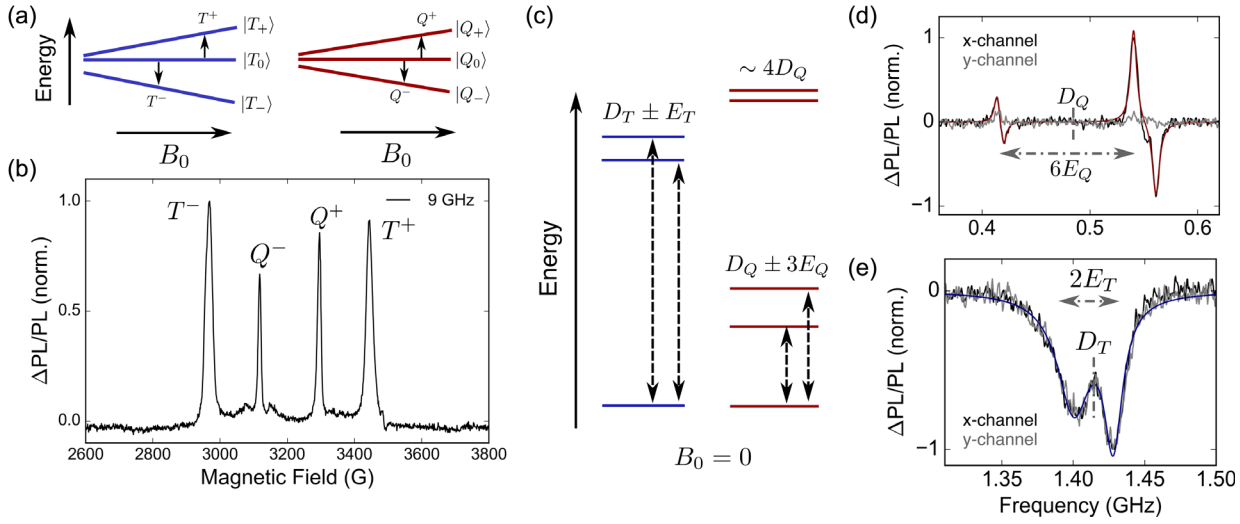


FIG. 2. Field-swept and zero-field ODMR of the triplet-pair state. (a) Energy levels of the uncoupled triplet and coupled quintet $m = 0, \pm 1$ sublevels as a function of field referenced to the $m = 0$ states $|T_0\rangle$ and $|Q_0\rangle$, respectively, with transitions at 9 GHz marked with arrows to correspond to experimentally observed transitions in (b). (b) ODMR spectrum at 9 GHz showing inner quintet transitions ($Q^{\pm}$) and outer triplet transitions ($T^{\pm}$). (c) Energy level diagram of triplet and quintet zero-field spin sublevels. Zero-field ODMR spectra with quintet transitions (d) marked with corresponding zero-field splitting parameters ($D_Q$, $E_Q$) and simulation in red and triplet transitions (e) marked with corresponding triplet parameters ($D_T$, $E_T$) and simulations in blue.

determine the corresponding orientations of the principal axes. The experimental ODMR maps for quintet and triplet states are shown in Fig. 3(c),(f). The observed resonances in Fig. 3(c) cannot be fit by a spin-1 state, which further confirms the assignment of the quintet state (see Supplemental Material [35]). We parameterize the orientation of the principal axes relative to the magnetic field with the polar angle $\theta$ and azimuthal angle $\phi$ as shown in Fig. 3(b),(e). The orientation of the quintet fine-structure axes is obtained by fitting these maps with the spin transitions predicted by the fine-structure parameters determined at zero field with the orientation as input. There are 10 possible transitions between the five quintet spin sublevels [Fig. 3(a)], which are overlaid on the quintet ODMR map [Fig. 3(c)]. It should be noted that the visibility of transitions depends on populations and selection rules, and transitions 3, 4, 6, 7, and 9 are not clearly observed experimentally. We find that the quintet state is oriented with fixed $\theta_q = 90 \pm 5°$ between $\hat{z}_q$ and $\mathbf{B}_0$ and $\phi_q = 30 \pm 5°$ between $\hat{x}_q$ and $\mathbf{B}_0$.

The evolution of the triplet zero-field transitions ($\sim$1.4 GHz) with field shown in Fig. 3(f) are consistent with $\theta_t = 90°$ (simulated transitions shown in black). We also observe $\theta_t \sim 0$ peaks due to a weak powder background, which decays quickly with field. The dominant $\theta_t = 90°$ triplet orientation correlates with the high-field spectrum [Fig. 2(b)]: triplet peaks are separated in field by $\sim hD/g\mu_B$, which occurs when $\theta_t \sim 90°$, whereas no peaks are observed for $\theta_t \sim 0$ (separation in field of $\sim 2D/g\mu_B$). Note that the transitions are consistent with $\phi_t \sim 0$, but this angle could not be extracted reliably and is not required for subsequent analysis because the triplet states are nearly axially symmetric (i.e., $E_T \approx 0$). As the $D$-tensor principal values and axes in the laboratory frame are obtained from a crystalline sample aligned with $\mathbf{B}_0 \| \hat{c}$, we can now compare them with the theoretically predicted $D$ tensors in the TIPS-tetracene crystal structure.

There are six potential nearest-neighbor dimer configurations in the TIPS-tetracene crystal structure [see Fig. 1(c)] and for each we can calculate the fine-structure parameters $(D_Q, E_Q, \theta_q, \phi_q)$ using Eq. (4) and the point-dipole approximation, the dipolar axes shown in Fig. 1(b), and the intermolecular distances extracted from the crystal structure [40]. The full set of values are summarized in the Supplemental Material [35]. The observed quintet parameters and extracted angles of $\theta_q \simeq 90°$ and $\phi_q \simeq 30°$ are consistent with exchange-coupled triplets localized either on molecules 1 and 2 [highlighted in blue in Fig. 1(c)] or on molecules 3 and 4 [molecules labeled and highlighted in green in Fig. 1(c)]. (We note that the transitions associated with the two dimers overlay with $\mathbf{B} \| \hat{c}$, but become distinct for $\mathbf{B} \perp \hat{c}$ as described theoretically and confirmed experimentally in the Supplemental Material.) The extracted local quintet fine structure is visualized in Fig. 4, where the full quintet and triplet dipolar interactions are shown with respect to the magnetic field in the lab frame and crystallographic axes, summarizing the local structure of quintet and triplet states in TIPS-tetracene and their relation to intermolecular geometry. [Note that the projection shown in Fig. 4 is rotated with respect to the projection used in the crystal structure

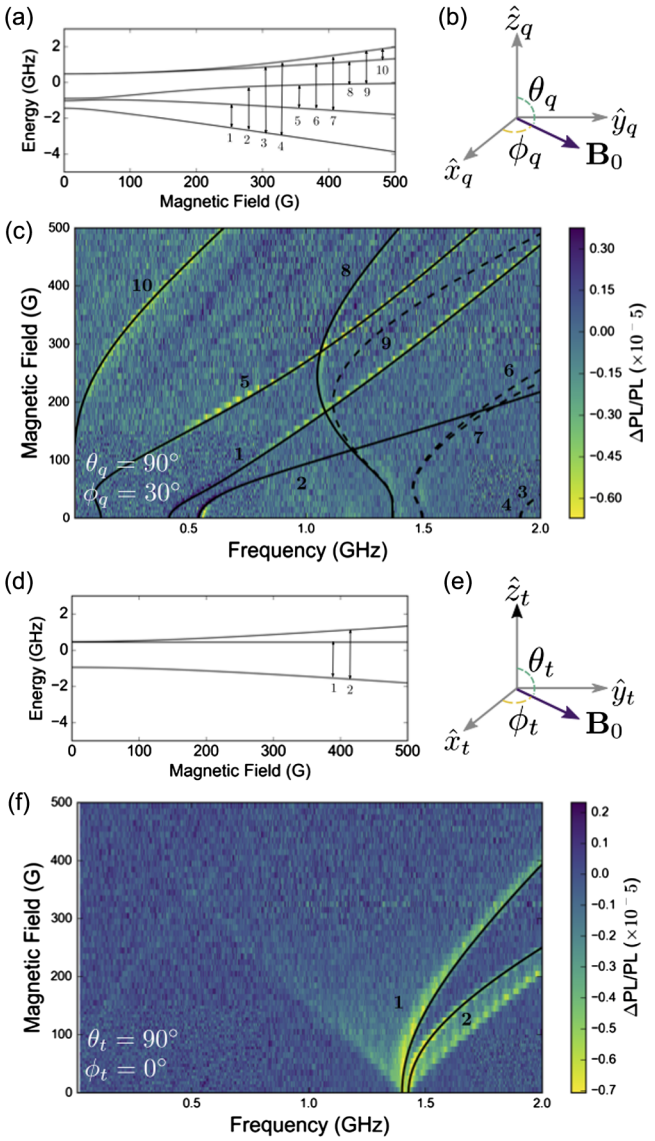


FIG. 3. Fine-structure tensors from broadband ODMR. (a), (d) Energy level diagram for the quintet (a) and triplet (d) states as a function of magnetic field. Arrows indicate potential transitions, corresponding to lines in (c) and (f) respectively. (b),(e) Schematic representation of the orientation of $\mathbf{B}$ in the quintet (b) and triplet (e) fine-structure axes. (c) ODMR transitions associated with the quintet state with overlay of simulated transitions. Signal has been isolated by subtracting a scaled out-of-phase (Y)-channel signal from the in-phase signal to remove triplet contributions. Black lines show simulations given for $\theta_q = 90°$ and $\phi_q = 30°$ with an uncertainty of $\pm 5°$ where solid (dashed) lines overlay (un-)observed transitions. (f) Y-channel (out-of-phase) ODMR map of the triplet state with overlay of calculated transitions in black with $\theta_t = 90°$ and $\phi_t = 0$.

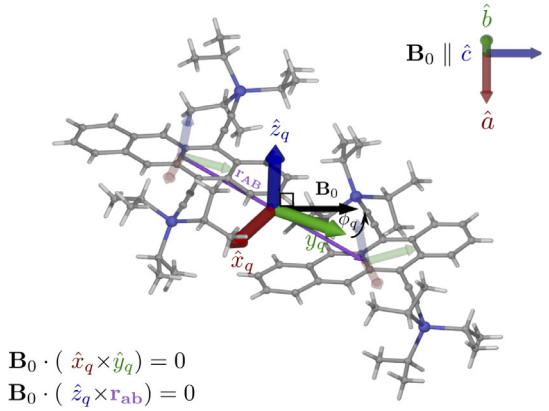


FIG. 4. Local geometry of the quintet fine-structure tensor in the TIPS-tetracene crystal (molecules 1 and 2) with crystal and magnetic field axes shown in the top right and with an angle of $\theta_q = 91.6°$ and $\phi_q = 30.6°$, where the crystal is oriented with $\mathbf{B}_0 \| \hat{c}$ with two coplanar triads of vectors, $(\hat{x}_q, \hat{y}_q, \mathbf{B}_0)$ and $(\hat{z}_q, \mathbf{r}_{ab}, \mathbf{B}_0)$.

shown in Fig. 1(c) and that while Fig. 4 highlights the dimer formed from molecules 1 and 2, the fine structure is equivalent up to a global rotation for the dimer formed of molecules 3 and 4.]

We have shown how the sensitivity of broadband magnetic resonance enables identification of triplet-pair geometries in a material with many possible intermolecular configurations. This approach is broadly applicable even in cases where the crystal structure is not known or relevant (as in disordered materials and devices with trap sites)—for example by expanding the present approach experimentally (e.g., incorporating the technique into a microscopy configuration) or theoretically (e.g., to describe statistical distributions of configurations). Here we find that the triplet pairs are localized on the closest $\pi$-stacked dimers of the crystal structure. As the fine structure is consistent with minimal modification from the ground state crystal structure, these results suggest that geometric reorganization is negligible in the quintet biexciton excited state. This description of the geometry of the triplet pair sets the foundation for time-resolved measurements to allow investigation of the transient localization and molecular reorganization of the pair state. While here we have examined a singlet fission material, this technique is broadly applicable to any device architecture with interacting excited states, from those incorporating two-dimensional materials and quantum dots to emerging hybrid organic-inorganic and bioengineered structures.

We are thankful for insightful discussions with H. Bouchiat and R. H. Friend and acknowledge support from ANR SPINEX and Labex ANR-10-LABX-0039-PALM. L. R. W. acknowledges support from Clare College, Cambridge. The authors declare no competing financial interests.

*Corresponding author.
chepelianskii@lps.u-psud.fr
†Corresponding author.
lrweiss@uchicago.edu
‡Present address: Pritzker School of Molecular Engineering, University of Chicago, Chicago, Illinois 60637, USA.

[1] G. W. Bryant, Phys. Rev. B **41**, 1243 (1990).
[2] G. Chen, T. Stievater, E. T. Batteh, X. Li, D. G. Steel, D. Gammon, D. S. Katzer, D. Park, and L. J. Sham, Phys. Rev. Lett. **88**, 117901 (2002).
[3] Y. Z. Hu, S. W. Koch, M. Lindberg, N. Peyghambarian, E. L. Pollock, and F. F. Abraham, Phys. Rev. Lett. **64**, 1805 (1990).
[4] M. A. Baldo, C. Adachi, and S. R. Forrest, Phys. Rev. B **62**, 10967 (2000).
[5] V. I. Klimov, D. W. McBranch, N. Barashkov, and J. Ferraris, Phys. Rev. B **58**, 7654 (1998).
[6] K. Masui, H. Nakanotani, and C. Adachi, Org. Electron. **14**, 2721 (2013).
[7] M. B. Smith and J. Michl, Chem. Rev. **110**, 6891 (2010).
[8] S. Singh, W. Jones, W. Siebrand, B. Stoicheff, and W. Schneider, J. Chem. Phys. **42**, 330 (1965).
[9] C. Swenberg and W. Stacy, Chem. Phys. Lett. **2**, 327 (1968).
[10] T. N. Singh-Rachford and F. N. Castellano, Coord. Chem. Rev. **254**, 2560 (2010).
[11] A. Rao and R. H. Friend, Nat. Rev. Mater. **2**, 17063 (2017).
[12] M. Hanna and A. Nozik, J. Appl. Phys. **100**, 074510 (2006).
[13] M. J. Tayebjee, A. A. Gray-Weale, and T. W. Schmidt, J. Phys. Chem. Lett. **3**, 2749 (2012).
[14] M. Einzinger, T. Wu, J. F. Kompalla, H. L. Smith, C. F. Perkinson, L. Nienhaus, S. Wieghold, D. N. Congreve, A. Kahn, M. G. Bawendi *et al.*, Nature (London) **571**, 90 (2019).
[15] D. N. Congreve, J. Lee, N. J. Thompson, E. Hontz, S. R. Yost, P. D. Reusswig, M. E. Bahlke, S. Reineke, T. Van Voorhis, and M. A. Baldo, Science **340**, 334 (2013).
[16] Y. Y. Cheng, T. Khoury, R. G. Clady, M. J. Tayebjee, N. Ekins-Daukes, M. J. Crossley, and T. W. Schmidt, Phys. Chem. Chem. Phys. **12**, 66 (2010).
[17] B. D. Ravetz, A. B. Pun, E. M. Churchill, D. N. Congreve, T. Rovis, and L. M. Campos, Nature (London) **565**, 343 (2019).
[18] R. S. Khnayzer, J. Blumhoff, J. A. Harrington, A. Haefele, F. Deng, and F. N. Castellano, Chem. Commun. **48**, 209 (2012).
[19] V. Gray, D. Dzebo, M. Abrahamsson, B. Albinsson, and K. Moth-Poulsen, Phys. Chem. Chem. Phys. **16**, 10345 (2014).
[20] Q. Liu, T. Yang, W. Feng, and F. Li, J. Am. Chem. Soc. **134**, 5390 (2012).
[21] Q. Liu, M. Xu, T. Yang, B. Tian, X. Zhang, and F. Li, ACS Appl. Mater. Interfaces **10**, 9883 (2018).
[22] M. J. Tayebjee, S. N. Sanders, E. Kumarasamy, L. M. Campos, M. Y. Sfeir, and D. R. McCamey, Nat. Phys. **13**, 182 (2017).
[23] L. R. Weiss, S. L. Bayliss, F. Kraffert, K. J. Thorley, J. E. Anthony, R. Bittl, R. H. Friend, A. Rao, N. C. Greenham, and J. Behrends, Nat. Phys. **13**, 176 (2017).
[24] D. Lubert-Perquel, E. Salvadori, M. Dyson, P. N. Stavrinou, R. Montis, H. Nagashima, Y. Kobori, S. Heutz, and C. W. Kay, Nat. Commun. **9**, 4222 (2018).

[25] Y. Matsui, S. Kawaoka, H. Nagashima, T. Nakagawa, N. Okamura, T. Ogaki, E. Ohta, S. Akimoto, A. Sato-Tomita, S. Yagi *et al.*, J. Phys. Chem. C **123**, 18813 (2019).
[26] S. Matsuda, S. Oyama, and Y. Kobori, Chem. Sci. **11**, 2934 (2020).
[27] S. L. Bayliss, L. R. Weiss, A. Mitioglu, K. Galkowski, Z. Yang, K. Yunusova, A. Surrente, K. J. Thorley, J. Behrends, R. Bittl *et al.*, Proc. Natl. Acad. Sci. U.S.A. **115**, 5077 (2018).
[28] S. L. Bayliss, L. R. Weiss, A. Rao, R. H. Friend, A. D. Chepelianskii, and N. C. Greenham, Phys. Rev. B **94**, 045204 (2016).
[29] J. A. Weil and J. R. Bolton, *Electron Paramagnetic Resonance: Elementary Theory and Practical Applications* (John Wiley & Sons, New York, 2007).
[30] H. Benk and H. Sixl, Mol. Phys. **42**, 779 (1981).
[31] S. A. Odom, S. R. Parkin, and J. E. Anthony, Org. Lett. **5**, 4245 (2003).
[32] H. L. Stern, A. Cheminal, S. R. Yost, K. Broch, S. L. Bayliss, K. Chen, M. Tabachnyk, K. Thorley, N. Greenham, J. M. Hodgkiss *et al.*, Nat. Chem. **9**, 1205 (2017).
[33] H. L. Stern, A. J. Musser, S. Gelinas, P. Parkinson, L. M. Herz, M. J. Bruzek, J. Anthony, R. H. Friend, and B. J. Walker, Proc. Natl. Acad. Sci. U.S.A. **112**, 7656 (2015).
[34] T. Yago, K. Ishikawa, R. Katoh, and M. Wakasa, J. Phys. Chem. C **120**, 27858 (2016).
[35] See Supplemental Material at http://link.aps.org/supplemental/10.1103/PhysRevLett.125.097402 for further theoretical derivations and experimental details.
[36] R. Merrifield, J. Chem. Phys. **48**, 4318 (1968).
[37] M. Wakasa, T. Yago, Y. Sonoda, and R. Katoh, Communications Series B, Chemistry and chemical engineering / Faculty of Sciences, University of Ankara **1**, 1 (2018).
[38] K. Ishikawa, T. Yago, and M. Wakasa, J. Phys. Chem. C **122**, 22264 (2018).
[39] S. L. Bayliss, A. D. Chepelianskii, A. Sepe, B. J. Walker, B. Ehrler, M. J. Bruzek, J. E. Anthony, and N. C. Greenham, Phys. Rev. Lett. **112**, 238701 (2014).
[40] D. Eaton, S. Parkin, and J. Anthony, CCCDC, 10.5517/cc119qsv (2013).